Miner Petrol (2012) 104:177–195
DOI 10.1007/s00710-011-0185-3

ORIGINAL PAPER

Multi-stage metasomatism in the lithosphere beneath the Veneto Volcanic Province (VVP, Northern Italy)

Claudia Cannatelli

Received: 25 September 2011 / Accepted: 3 November 2011 / Published online: 7 December 2011

Abstract Mantle peridotites from the Veneto Volcanic Province (VPP) have been investigated in order to constrain P-T conditions of mantle events, determine the style of the metasomatic reactions, and the compositions of the metasomatic agents. Studied rocks show dominant protogranular and transitional textures; only one sample shows effect of pyrometamorphism. Clinopyroxenes in protogranular lherzolites show depleted LREE patterns, while those of transitional rocks are characterised by spoon-shaped REE patterns (La up to 60 times chondrite), and variable enrichments in LILE. Two generations of fluid inclusions are recognised: 1) Type I (CO_2 ± CO ± C fluid) found only in orthopyroxene of transitional xenoliths which may contain very small amphibole; 2) Type II (CO_2-rich fluid) found in all minerals of all xenoliths. Most of inclusions homogenize to liquid, with Th_L ranging between −44 and 31°C. The densest CO_2 fluid inclusions (d=1.13 g/cm^3), indicates a trapping pressure of ~10 kbar at 800°C. We propose that the mantle beneath the VVP equilibrated at pressures of 10 kbar, at about 800°C. Traces of an aqueous fluid preserved as fluid inclusions in orthopyroxene suggest the existence of an older subduction related metasomatic event and the occurrence of two stages metasomatism in the lithosphere beneath the SE Alps.

Editorial handling: B. De Vivo

C. Cannatelli (✉)
Centro de Vulcanologia e Avaliação de Riscos Geológicos,
Universidade dos Açores,
Rua Mãe de Deus,
9500-801 Ponta Delgada, Portugal
e-mail: claudia.cannatelli@azores.gov.pt

Introduction

Tertiary alkali-basalts of the Veneto Volcanic Province (VVP, SE Alps) contain abundant mantle xenoliths and represent a unique opportunity to study the mantle beneath northern Italy. Previous studies showed that peridotites consist of protogranular lherzolites and harzburgites, re-equilibrated under spinel-facies conditions (Morten 1987; Morten and Bondi 1981). Some authors (Siena and Coltorti 1989, 1993; Coltorti et al. 2000; Beccaluva et al. 2001; Bonadiman et al. 2001) have shown that the peridotites from this area are representative of variable degree of mantle depletion and subsequent enrichment, revealing a major metasomatic event by the presence of abundant interstitial glasses (strongly reacted xenoliths or pyrometamorphic). More recently Gasperini et al. (2006) suggested that the lithosphere under the VVP has been affected by two metasomatic events: an older one induced by slab-derived material related to Alpine Orogeny, followed by more recent alkaline metasomatic event consistent with the Tertiary volcanism of the area.

Present study reports the petrography, mineral chemistry, fluid and melts inclusions of selected peridotites from three localities of VVP: San Giovanni Ilarione quarry, Mt. Madarosa and Mt. di Gloso. Studied rocks consist of protogranular and transitional (this last one described for the first time) lherzolites and harzburgites, with limited or no evidence of pyrometamorphism. These rocks were carefully selected to study mantle evolution prior the infiltration of melts related to the Tertiary volcanism, in order to characterize the petrological and geothermobarometric history of the lithosphere in this area prior the petrogenesis of VVP alkali basalts.

Geological setting

The VVP is located in Northeastern Italy, SE of the Southern Alps sector (Fig. 1). During the Tertiary, convergence between Africa and Europe induced a subduction of the European plate underneath the African plate, forming a district where the magmatic activity extended over 1,500 km^2 (De Vecchi et al. 1976; De Vecchi and Sedea 1995). The VVP magmatism occurred in several stages, starting with the sporadic eruption of Na-alkaline lamprophyre dikes in the Late Cretaceous (Galassi et al. 1994), with the main volcanic events occurring between Late Paleocene and Oligocene (De Vecchi and Sedea 1995). The VVP volcanic activity can be related to the foreland reaction to the Alpine orogenic phase and is considered to have a "within-continental-plate" signature (De Vecchi and Sedea 1995; De Vecchi et al. 1976; Piccoli et al. 1981; Barbieri et al. 1982, 1991).

The magmatic activity in the VVP developed in about 35 Ma (De Vecchi and Sedea 1995) and was not continuous, spanning in 1–3 Ma time period (Barbieri et al. 1982) with an apex in the middle Eocene (De Vecchi and Sedea 1995). The volcanic products span among (mela)-nephelinites, basanites, alkaline basalts, transitional basalts and tholeiites (Bianchini et al. 2008). Incompatible element patterns and Sr-Nd-Pb isotopic composition of the most primitive basalt show a prevalent HIMU and DMM-like mantle source (Siena and Coltorti 1989; Beccaluva et al. 2001; Macera et al. 2008).

On the basis of different tectonic and magmatic characteristics the VVP can be divided in three sectors: 1–2) Mts. Lessini (Western and Eastern), delimited by the Castelvero and Schio-Vicenza tectonic lines (Fig. 1). In this area, the magmatic activity occurred from Upper Paleocene to the Upper Oligocene (Barbieri et al. 1982) and the volcanic products consist of tuffs, pillow lavas, lavas flows and eruptive necks with compositions spanning among nephelinic, basanitic, alkali basalt, transitional basalt and tholeiitic (Bonadiman et al. 2001); 3) Marostica Hills, delimited to the west by the Schio-Vicenza tectonic line (Fig. 1) and to the east by the Brenta River. In this area the magmatic activity occurred during the Oligocene and was mostly effusive, with sporadic subaerial episodes related to several necks. The most abundant products are transitional and tholeiitic basalts, even though basanite and alkali basalt are still present (Bonadiman et al. 2001).

For this study, the xenoliths were collected in all three sectors, in particular Mt. Gloso (MG) outcrop for the Marostica Hills area and Mt. Madarosa (MMad) and San Giovanni Ilarione (SGIL) outcrops for the Mts. Lessini sectors.

Analytical techniques

Chemical analysis of bulk rocks was performed at the University of Siena (Italy) by X-ray fluorescence (XRF)

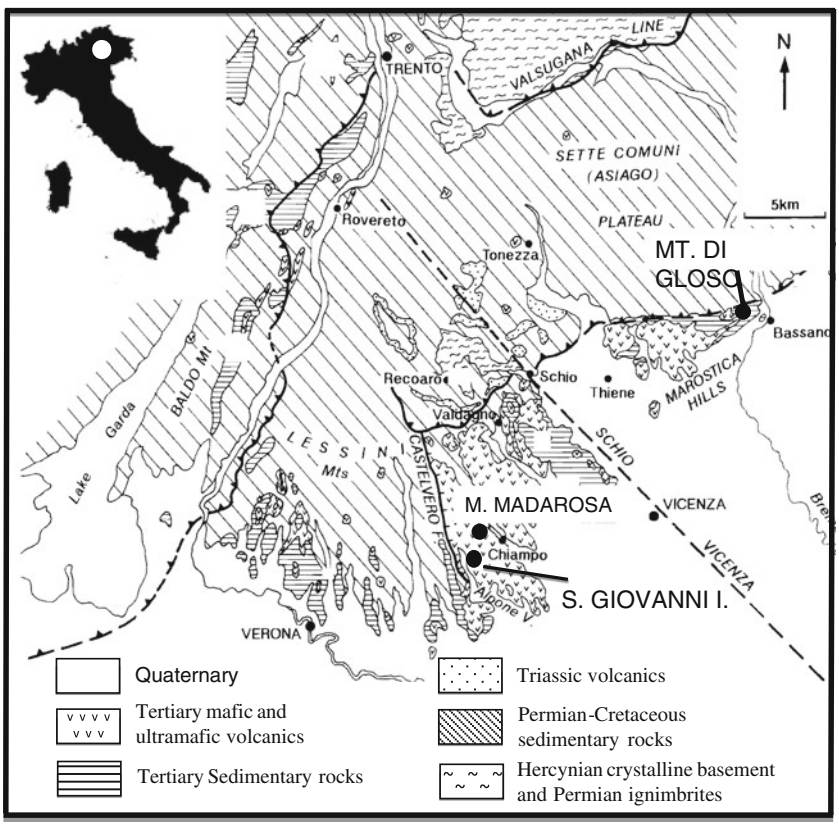

Fig. 1 Simplified geological sketch map of VVP (modified from De Vecchi and Sedea 1995). The three sampling localities are indicated with star symbol

using a Philips MagicX Pro PW. Loss on ignition was determined by heating the samples at 1,050°C for 2 h. The background and mass absorption intensities are calculated against the calibrations constructed from 24 international geological reference materials.

Fluid inclusion studies were performed at the University of Siena (Italy) by a Linkam TH600 heating and cooling stage, on doubly polished sections of about 100 μm thickness. SYNFLINC® standard synthetic fluid inclusions were used to calibrate the stage, checking the temperature at CO_2 (−56.6°C) and H_2O (0°C) triple points. Accuracy at standard points was estimated ±0.1°C. Fluid density was calculated using software package by Bakker (2003) and equation of state by Holloway (1977) for pure CO_2, CO_2 + CO mixtures, and CO_2 + H_2O ± CO. Raman spectroscopy analyses were performed by a Labram multichannel spectrometer of Jobin-Yvon Ltd. at the Dipartimento di Scienze della Terra, University of Siena (Italy). The source of excitation was an Ar^+ laser producing a line at 514.5 nm. Raman intensities were measured with a Peltier-cooled CCD detector and the beam was focused at a spot size of about 1–2 μm, using an Olympus 100x lens (Frezzotti et al. 2011). The scattered light was analysed using a Notch holographic filter with spectral resolution of 1.5 cm^{-1} and grating of 1.800 grooves/mm.

Mineral major elements were analysed with a CAMECA SX 50 electron microprobe at IGAG-CNR in Rome (Italy), operated at an acceleration voltage of 15 kV and a probe current of 15 nA. For glasses, conditions of measurements were 15 keV accelerating voltage, 4 nA beam current, 20 μm diameter of electron beam, counting times 10–20 s. Sodium was analyzed first to minimize alkali-loss. Mineral analyses were always assisted by back-scattered electron (BSE) images to control the microtextural site. Natural and synthetic silicates were used as standards. Chemical analyses of minerals were also performed by Philips XL30 scanning electron microscopy (SEM) at the University of Siena (Italy), equipped with an energy-dispersive spectrometer. Analytical conditions include an accelerating voltage of 20 kV and beam current of 23–25 nA.

The LA ICP-MS analyses were performed at the Department of Earth Science, University of Perugia (Italy), using a Thermo Electron X7 equipped with a quadruple based ICP-MS. Spot sizes of 60 μm were used for mineral phases; counting time was 40 s for the background and 60 s for sample analyses. Calibration was performed using NIST SRM612 as external calibration sample in conjunction with internal standardization, following the method of Longerich et al. (1996). Precision is better than 10% for all elements, except for Pb (~15%). Details on the analytical method can be found in Petrelli et al. (2007, 2008).

Xenoliths and hosted glass petrography

Seventeen best preserved samples, from more than 50 xenoliths collected in three localities of the VVP (Mt. Madarosa, San Giovanni Ilarione and Mt. Gloso), were selected for our studies. They consist of a four–phase assemblage: clear olivine (43–70% vol.), light brown orthopyroxene (20–42% vol.), green clinopyroxene (5–15% vol.) and brown spinel (2–8% vol.) calculated using bulk rock chemistry (CIPW Norm Calculation Program) and correction factors for ultramaphic rocks. The great majority of xenoliths cluster in the spinel - lherzolite field; only one sample (MMad7a) is a spinel - harzburgite (Fig. 2). The xenoliths are generally angular and range between 2 and 5 cm in size, with a few samples up to 10 cm in diameter. Hydrous phases (e.g. amphibole, phlogopite, etc.) are absent in VVP xenoliths, although previous works indicate that traces of amphibole may locally be present (Morten 1979). Xenoliths were chosen among samples showing dominant protogranular and transitional (intermediate between protogranular and porphyroclastic) textures. Although protogranular and pyrometamorphic textures have been already described in VVP (Morten 1979; Bonadiman et al. 2001; Beccaluva et al. 2001), transitional rocks have never been investigated.

Protogranular xenoliths

Protogranular xenoliths (following the classification of Mercier and Nicolas 1975) consist of coarse and deformed grains of olivine and orthopyroxene (~1–8 mm), with minor interstitial clinopyroxene and spinel (Fig. 3a). Generally, olivine is kinked and shows curved boundaries, and in some cases, include small rounded pyroxene grains. Orthopyroxene has smooth and curved boundaries, often is kinked and usually contains exsolution lamellae of clinopyroxene and/or rounded spinel grains. Clinopyroxene is always small (0.5–1 mm) with irregular shape, in general interstitial. In some cases, clinopyroxene contains exsolution lamellae of orthopyroxene and/or rounded spinel grains. Few clinopyroxenes show partial sieve texture. Spinel has vermicular shape (< 2 mm) inside the orthopyroxene (Fig. 3b) or between the orthopyroxene and clinopyroxene; in some cases it is zoned with a brown core and dark rim and is surrounded by silicate phases. Spinel is never found enclosed in olivine grains.

Transitional xenoliths

Most selected lherzolites and harzburgites have transitional texture (Fig. 3c and d), intermediate between protogranular and porphyroclastic (Mercier and Nicolas 1975). They consist of two generations of olivine and orthopyroxene.

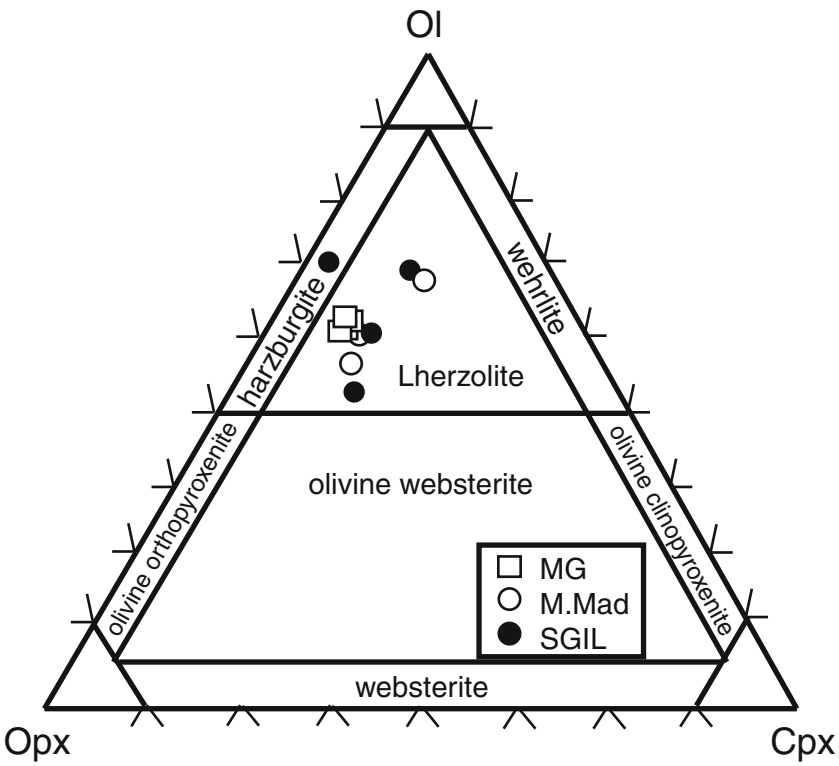

Fig. 2 Classification (based on chemical analysis, see text for details) of selected mantle xenoliths from VVP

Primary minerals appear as coarse deformed (kinked and/or strained) porphyroclasts (~1–8 mm), and secondary minerals as smaller, equigranular neoblasts, often forming triple joints (~0.1–0.5 mm). The primary orthopyroxene generally shows exsolution lamellae of clinopyroxene, abundant fluid inclusions, and may show resorption at the rims. Transitional xenoliths are characterised by high normative orthopyroxene. Clinopyroxene (~0.5–1 mm) is commonly characterised by exsolution of orthopyroxene lamellae and/or spinel; often clinopyroxene shows a porous rim of variable thickness (partial sieve texture) and a clear core (sometimes interested by cross-cutting veinlets and irregular patches) with abundant fluid and melt inclusions. Small neoblasts of clinopyroxene are rarely present (<0.5 mm). Spinel has vermicular shape, when in contact with orthopyroxene (as in protogranular texture), and the characteristic holly-leaf shapes, when surrounded by olivine. Idiomorphic spinel is also present. Transitional xenoliths contain abundant fluid and melt inclusions.

Strongly reacted xenolith

Both protogranular and transitional xenoliths are interested by melt infiltration to variable extents (Fig. 3e). Such a late process is very well known in mantle rocks from this area (i.e. pyrometamorphic textures described by Siena and Coltorti 1989; Beccaluva et al. 2001; Bonadiman et al. 2001). In the present study, only one xenolith (SGIL7a) showed strong reaction with a melt phase (i.e. pyrometamorphism) and it was selected as representative of its kind. SGIL7a is a transitional spinel lherzolite containing abundant glass (5–8% vol.) as microveins (~1 mm in thickness), glassy pockets and blebs (<500 μm in diameter) with variable degree of crystallization. In this rock, clinopyroxene generally shows no exsolution, shows sieve texture and micro-channels optically-continuous with interstitial porous areas that might be void or filled by glass. Spinel also show sieve texture, characterized by coronae (containing microlites of olivine and/or clinopyroxene) and it is often in contact with sieve-clinopyroxenes.

Glass

Protogranular and transitional xenoliths contain glass as microveins, pockets and melt inclusions (<1 vol.%). Glass microveins are present within the xenoliths, and are never in contact with the host basalt. Based on textural features two types of melt/glass have been distinguished:

– Type A glass, in olivine and orthopyroxene, forming a quite complex network of microveins and trails of melt inclusions (± CO_2) and connecting in interstitial pockets. The microveins (<50 μm in thickness) are inter- or intra- granular and contain colourless glass. Glass pockets can reach 0.5 mm of diameter and are usually in contact with orthopyroxene and olivine and may contain skeletal crystals of plagioclase ± olivine ± clinopyroxene set in a glassy, colourless to pale-brown

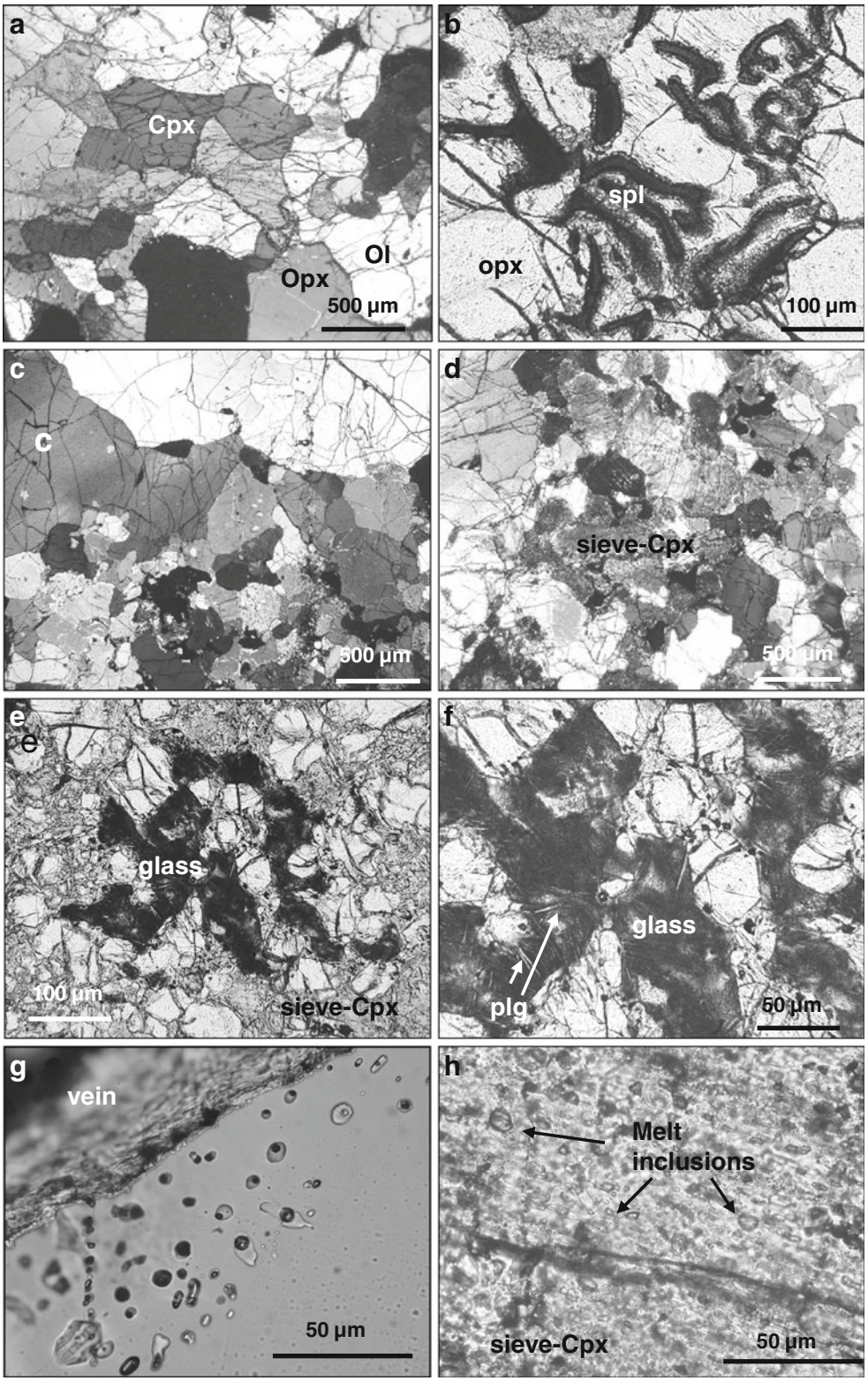

Fig. 3 Microphotographs of thin sections of mantle xenoliths: **a**) protogranular texture, showing coarse and deformed grains of olivine and orthopyroxene with minor interstitial clinopyroxene and spinel; **b**) spinel grain with vermicular shapes inside the orthopyroxene in protogranular texture (crossed polars); **c**) transitional texture with coarse deformed grains and neoblasts; **d**) sieve-clinopyroxenes in a transitional xenolith; **e**) glass bleb and sieve-clinopyroxene in pyrometamorphic xenolith; **f**) enlargement of glass bleb showed in **e**), associated with plagioclase; **g**) Type A melt inclusions ± CO_2; h) Type B melt inclusions in sieve-clinopyroxene

groundmass (Fig. 3f). Type A melt inclusions are sometimes associated to CO_2 fluid inclusions, occur in trails or in small clusters within single crystals, are transparent and consist of glass ± one or more gas bubbles. The size of Type A melt inclusions is less than 50 µm (Fig. 3g) and the shape varies from rounded to irregular.

– Type B glass is restricted to sieve-clinopyroxene grains, where it forms colourless short micro-channels (~100 µm) around the porous rims, sometimes in

Table 1 Selected chemical analyses of olivine from VVP xenoliths

Rock Texture Sample	Lherz. Pr M.Mad. 22b-4,1	Lherz. Pr M.Mad. 22b-1,6	Lherz. Pr M.Mad. 27-2a-6a	Lherz. Pr M.Mad. 27-2a-6b	Lherz. Pr M.Mad. 28-1h	Lherz. Pr M.Mad. 28-5c	Lherz. Pr M.Mad. 30-3d	Lherz. Tr M.Mad. 35-2-4d	Lherz. Tr SGIL 2a-9,2	Lherz. Tr SGIL 2a-11,6	Lherz. Tr SGIL 2b-1,11
(wt%)											
SiO2	40.43	40.79	41.14	41.42	41.05	41.36	40.87	40.75	41.61	40.93	40.49
Cr2O3	0.12	0.00	0.00	0.00	0.00	0.04	0.00	0.00	0.01	0.09	0.19
FeOtot	10.00	10.32	9.90	9.77	10.45	10.09	10.42	9.13	9.10	8.52	9.08
MnO	0.11	0.15	0.15	0.04	0.11	0.26	0.16	0.25	0.12	0.14	0.16
NiO	0.35	0.26	0.42	0.40	0.35	0.38	0.46	0.44	0.42	0.39	0.31
MgO	48.80	48.88	48.46	48.15	47.97	47.82	48.08	49.48	49.12	49.98	49.85
CaO	0.05	0.10	0.01	0.02	0.03	0.01	0.00	0.03	0.01	0.25	0.16
Sum	99.88	100.50	100.08	99.81	99.99	99.96	100.03	100.09	100.38	100.28	100.22
Fo%	89.69	89.41	89.71	89.79	89.10	89.41	89.16	90.62	90.59	91.28	90.73
Fa%	10.31	10.59	10.29	10.21	10.90	10.59	10.84	9.38	9.41	8.72	9.27
mg*	0.897	0.894	0.897	0.898	0.891	0.894	0.892	0.906	0.906	0.912	0.907
	Lherz. Tr SGIL 2b–1,11	Lherz. Tr SGIL 2b–1,5	Lherz. Tr SGIL 2b–1,9	Lherz. Py SGIL 7a–6,1	Lherz. Py SGIL 7a–5,1	Lherz. Py SGIL 7a–8,4	Lherz. Py SGIL 7a–1,1	Harzb. Tr M.Mad. 7a–4,1	Harzb. Tr M.Mad. 7a–4,2	Harzb. Tr M.Mad. 7a–4,4	Harzb. Tr M.Mad. 7a–3,4
(wt%)											
SiO2	40.49	40.41	40.87	40.43	39.45	39.89	40.11	40.27	39.54	40.23	40.43
Cr2O3	0.19	0.04	0.03	0.01	0.00	0.02	0.00	0.03	0.06	0.03	0.00
FeOtot	9.08	9.27	8.75	10.66	14.28	13.06	12.72	9.73	11.20	9.42	9.19
MnO	0.16	0.12	0.14	0.19	0.21	0.26	0.10	0.22	0.14	0.13	0.20
NiO	0.31	0.44	0.34	0.32	0.29	0.30	0.44	0.43	0.30	0.39	0.45
MgO	49.85	49.57	49.93	48.69	46.40	47.11	46.81	49.40	48.22	49.59	50.26
CaO	0.16	0.09	0.00	0.05	0.10	0.08	0.16	0.04	0.21	0.06	0.00
Sum	100.22	99.96	100.08	100.35	100.74	100.71	100.33	100.12	99.68	99.86	100.53
Fo%	90.73	90.51	91.05	89.06	85.28	86.54	86.78	90.05	88.47	90.37	90.70
Fa%	9.27	9.49	8.95	10.94	14.72	13.46	13.22	9.95	11.53	9.63	9.30
mg*	0.907	0.905	0.910	0.891	0.852	0.865	0.867	0.900	0.884	0.904	0.907

*mg** Mg/(Mg + Fetot); *Pr* protogranular texture; *Tr* transitional texture; *Py* pyrometamorphic texture

Table 2 Selected chemical analyses of clinopyroxene from VVP xenoliths

Rock texture sample	Lherz. Pr M.Mad. 1a3-cpx1	Lherz. Pr M.Mad. 22b1-cpx2	Lherz. Pr M.Mad. 27-2a-1a	Lherz. Pr M.Mad. 30-3e	Lherz. Tr M.Mad. 35-2-4e	Lherz. Tr SGIL 2a-11,4	Lherz. Tr M.Mad. 1a-5,11	Lherz. Tr MG 14d2-cpx1	Lherz. Tr MG 14d2-cpx2	Lherz. Tr MG 14d2-cpx3	Lherz. Tr SGIL 7a-2,2	Lherz. Tr SGIL 7a-4,5	Lherz. Tr SGIL 7a-5,2	Lherz. Py SGIL 7a1-cpx1	Lherz. Py SGIL 7a2-cpx1	Harz. Tr M.Mad. 7a2-cpx1	Harz. Tr M.Mad. 7a2-cpx2	Harz. Tr M.Mad. 7a2-cpx3	Harz. Tr M.Mad. 7a1-cpx2
(wt%)																			
SiO2	52.04	52.58	51.78	51.40	51.39	52.72	52.60	52.44	51.90	51.83	50.74	50.51	50.07	51.24	51.73	52.84	52.69	52.91	53.09
Al2O3	6.92	6.07	6.78	6.95	6.71	2.88	0.69	6.25	6.42	6.41	7.34	7.17	7.32	7.32	6.82	4.86	4.69	4.90	4.44
TiO2	0.40	0.38	0.44	0.39	0.48	0.11	0.25	0.49	0.50	0.41	0.45	0.87	0.67	0.40	0.44	0.07	0.06	0.02	0.05
Cr2O3	1.13	0.79	1.14	0.92	1.11	0.80	1.17	0.74	0.79	0.92	0.82	0.90	0.76	0.94	0.74	1.10	1.17	1.08	1.03
FeOtot	2.36	2.50	2.36	2.89	2.22	2.18	2.55	3.35	3.42	3.83	4.28	4.89	4.60	2.83	2.90	2.09	2.55	2.01	2.47
MnO	0.07	0.09	0.11	0.12	0.00	0.00	0.04	0.12	0.04	0.13	0.04	0.07	0.06	0.10	0.02	0.07	0.00	0.07	0.10
NiO	0.15	0.05	0.01	0.06	0.01	0.10	0.00	0.09	0.06	0.06	0.01	0.06	0.01	0.08	0.05	0.00	0.03	0.03	0.03
MgO	14.37	14.54	13.92	14.73	13.91	17.08	18.83	15.26	15.23	15.16	14.93	15.65	14.91	14.65	14.49	15.23	15.47	15.40	15.62
CaO	21.59	22.11	21.62	21.54	21.47	23.62	21.42	20.43	20.51	20.31	20.60	18.94	19.85	20.16	21.00	22.32	22.49	22.00	22.16
Na2O	1.65	1.38	1.70	1.21	1.76	0.52	0.75	1.46	1.33	1.38	1.39	1.25	1.47	1.42	1.39	1.16	1.09	1.23	0.96
Sum	100.67	100.50	99.87	100.20	99.05	100.00	98.30	100.63	100.18	100.43	100.60	100.31	99.70	99.13	99.59	99.79	100.24	99.66	99.96
Wo%	49.66	49.85	50.37	48.53	50.45	48.13	43.16	46.04	46.20	45.65	46.03	42.47	44.88	47.08	48.33	49.38	48.89	48.84	48.29
En%	45.99	45.60	45.13	46.19	45.47	48.41	52.78	47.85	47.72	47.40	46.43	48.84	46.89	47.59	46.41	46.88	46.77	47.56	47.34
Fs%	4.35	4.55	4.51	5.28	4.08	3.46	4.07	6.10	6.08	6.95	7.54	8.69	8.23	5.33	5.26	3.74	4.34	3.60	4.37
mg*	0.916	0.912	0.913	0.901	0.917	0.933	0.929	0.890	0.888	0.876	0.861	0.850	0.852	0.902	0.899	0.928	0.915	0.931	0.918
(ppm)																			
K		41.5						41.5								166.02		41.5	
Ti	2400	2280						2940	3000	2460					2640	420	360	120	300
Sc	55.64	62.92						64.50	66.77	78.39					66.13	57.35	64.21	53.13	58.74
V	206.24	207.16						196.91	206.87	208.28					227.77	179.62	197.96	213.71	190.74
Cr	6597.39	5067.43						4667.79	5334.60	4601.13					5255.87	6633.03	6446.18	8159.09	6355.30
Ga	3.46	3.62						3.47	4.10	3.54					3.80	1.93	2.01	3.62	2.08
Rb	<0.070	<0.096						0.40	<0.062	0.20					<0.062	<0.057	0.09	0.19	<0.057
Sr	4.60	6.91						25.94	66.87	138.98					11.87	14.35	46.40	23.36	44.75
Y	14.98	18.66						21.93	22.42	19.80					18.58	5.55	5.16	4.93	4.63
Zr	7.11	8.80						13.32	14.42	19.26					11.53	1.29	1.24	1.02	1.17
Nb	0.07	<0.040						0.30	0.44	0.93					7.51	0.69	0.24	0.57	0.12
Cs	<0.046	<0.065						0.07	<0.042	<0.037					<0.043	0.06	0.05	<0.048	<0.037
Ba	<0.176	<0.27						0.22	<0.171	0.50					0.74	<0.171	2.60	0.48	0.26
La	0.04	<0.023						1.81	5.89	9.91					1.02	1.20	8.19	3.39	9.14
Ce	0.20	0.38						1.27	6.88	18.54					1.47	1.05	9.12	3.79	6.99
Pr	0.15	0.20						0.31	0.75	2.39					0.26	0.11	0.68	0.26	0.40
Nd	1.57	2.18						2.71	3.81	9.64					2.16	0.48	1.46	0.81	0.78
Sm	1.02	1.37						1.54	1.53	2.24					1.12	0.10	0.18	0.08	0.10
Eu	0.43	0.51						0.70	0.68	0.80					0.50	0.04	0.08	0.05	0.04

Table 2 (continued)

Rock texture sample	Lherz. Pr M.Mad. 1a3-cpx1	Lherz. Pr M.Mad. 22b1-cpx2	Lherz. Pr M.Mad. 27-2a-1a	Lherz. Tr M.Mad. 30-3e	Lherz. Tr SGIL 35-2-4e	Lherz. Tr M.Mad. 2a-11,4	Lherz. Tr MG 1a-5,11	Lherz. Tr MG 14d2-cpx1	Lherz. Tr MG 14d2-cpx2	Lherz. Tr MG 14d2-cpx3	Lherz. Tr SGIL 7a-2,2	Lherz. Tr SGIL 7a-4,5	Lherz. Tr SGIL 7a-5,2	Lherz. Py SGIL 7a1-cpx1	Lherz. Py SGIL 7a2-cpx1	Harz. Tr M.Mad. 7a2-cpx1	Harz. Tr M.Mad. 7a2-cpx2	Harz. Tr M.Mad. 7a2-cpx3	Harz. Tr M.Mad. 7a1-cpx2
Gd	1.50	2.33					2.97	2.77	2.72					1.94	0.23	0.31	0.32	0.28	
Tb	0.36	0.43					0.52	0.52	0.49					0.42	0.07	0.06	0.06	0.07	
Dy	2.59	3.33					4.05	3.93	3.88					3.32	0.67	0.69	0.51	0.57	
Ho	0.57	0.67					0.84	0.90	0.74					0.72	0.20	0.20	0.20	0.18	
Er	1.67	2.27					2.47	2.58	2.35					2.14	0.66	0.68	0.56	0.60	
Tm	0.24	0.33					0.35	0.37	0.33					0.31	0.12	0.11	0.11	0.09	
Yb	1.65	2.08					2.41	2.36	2.10					1.86	0.74	0.91	0.83	0.74	
Lu	0.24	0.29					0.35	0.34	0.32					0.28	0.13	0.12	0.12	0.14	
Hf	0.44	0.55					0.75	0.70	0.87					0.51	0.03	0.04	0.05	<0.025	
Ta	0.01	<0.0132					<0.0057	0.01	0.11					0.07	0.04	0.02	0.02	0.02	
Pb	0.08	<0.0181					0.21	0.24	0.23					0.06	0.31	0.60	0.45	0.72	
Th	0.01	<0.0058					1.23	1.36	1.19					0.50	0.34	1.45	0.78	1.26	
U	0.0078	0.0022					0.298	0.223	0.169					0.095	0.163	0.338	0.315	0.437	

*mg** Mg/(Mg + Fetot), *Pr* protogranular texture, *Tr* transitional texture, *Py* pyrometamorphic texture

contact with olivine and spinel; Type B glass is also present as transparent primary rounded melt inclusions (<50 μm) ± CO_2 bubbles (Fig. 3h), concentrated in the cores of sieve-clinopyroxene. In glassy Type B traces (<1 vol.%) of prismatic apatite and illmenite are detected by back-scattered electron (BSE) imaging.

Mineral chemistry

Major elements

In protogranular and transitional lherzolites and harzburgite, olivine is $Fo_{88.47–91.28}$ with NiO content between 0.26 and 0.48 wt%, and Cr_2O_3 up to 0.19 wt% (Table 1). In transitional rocks no difference is observed between neoblasts and porphyroclasts.

Clinopyroxene is a Cr-diopside ($Wo_{45.65–50.85}En_{44.80–49.50}Fs_{3.60–6.95}$) and shows variable compositional range (Table 2; Fig. 4). Clinopyroxene in lherzolites with protogranular and transitional textures shows Mg # [= Mg/(Mg + Fe^{tot})] between 0.896 and 0.923, TiO_2=0.33–0.51 wt%, Cr_2O_3=0.71–1.18 wt%, Al_2O_3=5.35–7.23 wt%, and Na_2O= 1.06–1.76 wt%. The clinopyroxene in the harzburgite shows slightly higher Mg # (0.909–0.931) and Cr_2O_3 values (0.84–1.26 w%), while TiO_2, Al_2O_3, Na_2O contents are lower (0.02–0.07 wt%, 3.67–5.00 wt%, 0.76–1.23 wt%, respectively). In protogranular lherzolites orthopyroxene is enstatite ($Wo_{0.54–2.34}En_{83.09–90.39}Fs_{8.71–14.57}$) with Mg # between 0.888 and 0.904, TiO_2=0.07–0.16 wt%, Cr_2O_3= 0.31–0.52 wt%, Al_2O_3=3.60–5.64 wt% and CaO=0.33–0.91 wt%. In transitional xenoliths orthopyroxene shows higher values of Mg# (0.905–0.912) and Cr_2O_3 contents (0.42–0.63 wt%), but similar TiO_2 (0.03–0.14 wt%), Al_2O_3 (3.60–4.78 wt%), and CaO (0.28–0.78 wt%) values. The orthopyroxene in the harzburgite shows similar Mg # (0.909), TiO_2 and CaO values, but lower Cr_2O_3 (0.32 wt%) and Al_2O_3 (3.06 wt%) contents than those present in lherzolites with transitional texture. (Table 3; Fig. 5)

In the protogranular and transitional lherzolites vermicular spinel is characterized by a variable Cr # [= Cr/(Cr + Al)] and Mg # (0.102–0.150 and 0.740–0.786, respectively) and high Al_2O_3 contents (52.83–57.01 wt%). In transitional lherzolites holly-leaf spinel has slightly higher Cr # (0.175–0.199), lower Mg # (0.697–0.733) and Al_2O_3 (47.39–49.34 wt%) values. The spinel in the harzburgite shows higher Cr # (0.188–0.245) and Mg # (0.798–0.860), but lower Al_2O_3 (19.28–42.06 wt%) content than those present in the lherzolites (Table 4; Fig. 6).

In the pyrometamorphic xenolith (SGIL7a) olivine shows lower and variable forsteritic values ($Fo_{86.78–89.06}$ for coarse grains; $Fo_{85.18–86.54}$ for neoblasts); clinopyroxene

($Wo_{42.14–48.33}En_{46.41–51.12}Fs_{5.19–6.75}$) has very similar values to those showed in protogranular lherzolites, with Mg # ranging between 0.886 and 0.905, TiO_2=0.39–0.54 wt%, Cr_2O_3=0.71–0.94 wt%, Al_2O_3=5.79–7.32 wt%, and Na_2O=1.20–1.67 wt%. Orthopyroxene presents lower Mg # (0.853–0.897), higher TiO_2 (0.10–0.32 wt%), and Al_2O_3 (4.13–5.90 wt%) contents respect to the protogranular lherzolite, and similar Cr_2O_3 (0.34–0.54 wt%), and CaO (0.56–1.20 wt%) values. Spinel shows variable composition in Cr # (0.089–0.162), Mg # (0.568–0.738), and Al_2O_3 (46.99–57.53 wt%) contents.

Trace elements

Clinopyroxenes in protogranular xenoliths show a depleted pattern of LREE [$(La/Yb)_n$=0.006–0.017], wheras MREE and HREE have a flat profile, with an average value of 10 times chondrite from Sm to Lu (Fig. 7a). Primary clinopyroxenes display strong depletion in incompatible elements with Nb, Sr, Zr and Pb below the detection limit (Fig. 7b). Transitional xenoliths (Fig. 7c) are characterised by variable enrichment in LREE [$(La/Yb)_n$=0.39–0.3.38], whereas the MREE and HREE show a flat pattern about 10–20 times chondrite. The transitional sample (MG14d, Fig. 7d) shows a depletion in Ba, an enrichment in Th, U and Sr, and light negative anomalies in Ti and Zr. The pyrometamorphic sample (SGIL7a, Fig. 7f) shows distinct trace element patterns, characterized by a depletion in Ba, an enrichment in Th and U, a strong positive anomaly in Nb and a light negative anomaly in Sr, Ti and Pb. In transitional harzburgite (Fig. 7g), the clinopyroxenes show enriched LREE content [$(La/Yb)_n$=1.16–12.13], a MREE depletion and a light enrichment in HREE (spoon-shaped pattern), about 3–4 times chondrite. In Fig. 7h a depletion in Rb, Ba, Ta and Nb, and a positive anomaly in Th and U can be observed, as well as a spoon-shaped pattern, with a depletion in HFSE and a significally enrichment in Sr and Pb.

Fluid inclusion study

Fluid inclusions in mantle xenoliths from VVP are observed in all the studied samples; they are abundant in transitional xenoliths and rare in protogranular and strongly reacted rocks. Based on textural characteristics two types of fluid inclusions are distinguished:

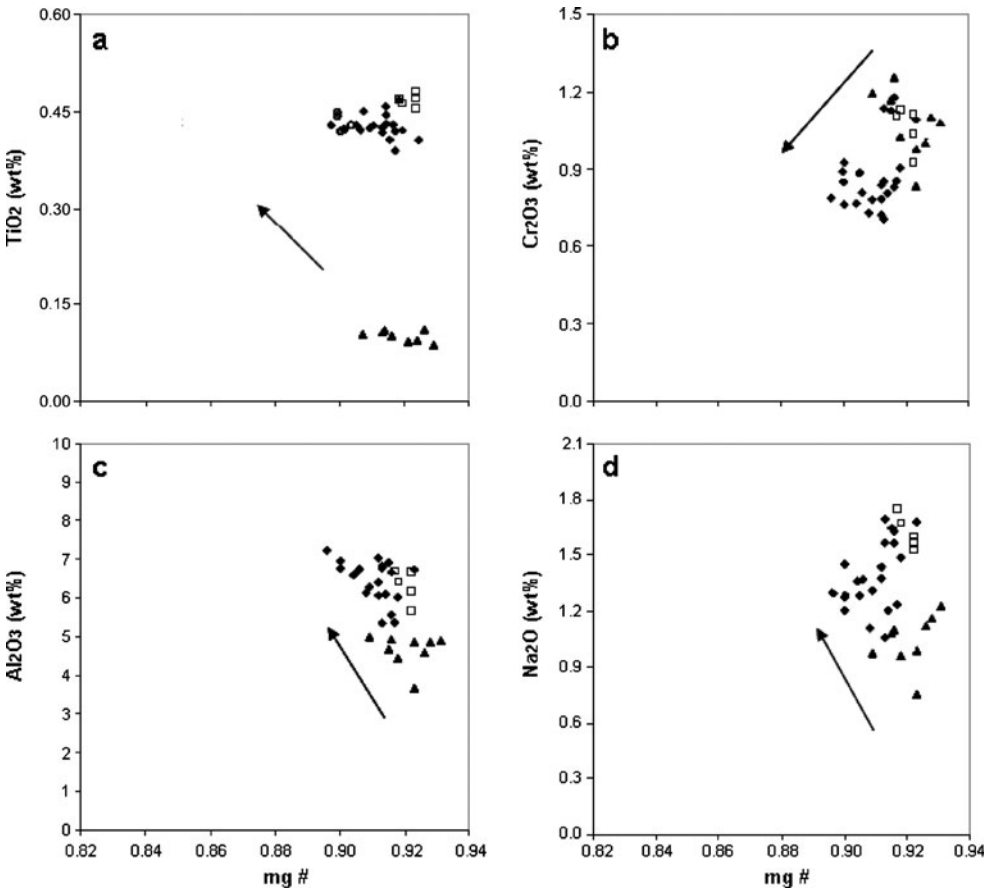

Fig. 4 TiO_2 – Cr_2O_3 – Al_2O_3 – Na_2O - mg # relationships in clinopyroxene in mantle xenoliths from VVP. Symbols: (*black diamond*) protogranular lherzolites; (*white square*) transitional lherzolites; (*black triangle*) transitional harzburgite

Table 3 Selected chemical analyses of orthopyroxene from VVP xenoliths

Rock	Lherz.	Lherz.	Lherz.	Lherz.	Lherz.	Lherz.	Lherz.	Lherz.	Lherz.	Lherz.	Lherz.	Lherz.	Lherz.	Lherz.	Lherz.	Lherz.	Lherz.	Lherz.	Lherz.	Harzb.
Texture	Pr	Pr	Pr	Pr	Pr	Pr	Pr	Pr	Pr	Tr	Tr	Tr	Tr	Tr	Tr	Tr	Py	Py	Py	Py	Tr
Sample	M.Mad. 1a-7,3	M.Mad. 22b-1,2	M.Mad. 28-2a	M.Mad. 28-2b	M.Mad. 28-3g	M.Mad. 28-1d	M.Mad. 28-1e	M.Mad. 28-1f	M.Mad. 30-1d	M.Mad. 35-2-5f	M.Mad. 35-2-6e	M.Mad. 35-2-3c	SGIL 2a-2,7	SGIL 2a-11,8	SGIL 2b-1,7	SGIL 2b-7,1	SGIL 7a-4,6	SGIL 7a-7,1	SGIL 7a-7,8	SGIL 7a-9,3	M.Mad. 7a-2,4
(wt%)																					
SiO2	54.34	54.67	54.18	54.38	54.94	55.34	54.08	55.43	54.85	55.57	54.90	54.66	54.98	54.85	55.06	55.19	54.60	54.26	54.68	53.99	55.38
Al2O3	4.93	4.40	5.03	5.64	4.91	4.52	5.51	4.12	4.83	3.92	4.75	4.55	4.13	4.03	3.60	4.07	4.13	4.78	4.78	5.25	3.06
TiO2	0.08	0.12	0.14	0.07	0.11	0.15	0.12	0.09	0.13	0.10	0.16	0.14	0.05	0.03	0.05	0.05	0.14	0.10	0.13	0.11	0.03
Cr2O3	0.52	0.49	0.46	0.46	0.44	0.34	0.47	0.36	0.40	0.43	0.53	0.45	0.59	0.42	0.50	0.63	0.38	0.45	0.41	0.49	0.32
FeOtot	6.40	6.41	6.76	6.98	6.81	6.90	6.44	7.16	6.96	5.98	5.87	6.04	5.78	5.91	6.05	5.88	7.28	6.71	6.80	8.00	6.12
MnO	0.14	0.04	0.22	0.16	0.12	0.25	0.16	0.24	0.19	0.14	0.15	0.21	0.05	0.24	0.16	0.16	0.17	0.09	0.15	0.18	0.17
NiO	0.10	0.07	0.14	0.03	0.11	0.08	0.14	0.02	0.05	0.05	0.06	0.10	0.05	0.09	0.09	0.13	0.04	0.16	0.08	0.07	0.09
MgO	33.51	33.03	31.81	31.21	31.14	32.29	31.20	32.67	31.97	33.26	31.52	32.83	33.87	33.85	33.97	33.48	32.74	32.87	32.65	31.91	34.35
CaO	0.36	0.75	0.91	0.81	1.57	0.72	1.62	0.33	0.52	0.47	1.67	0.62	0.60	0.42	0.31	0.28	0.56	0.71	0.72	0.73	0.44
Na2O	0.04	0.03	0.04	0.06	0.13	0.07	0.05	0.02	0.03	0.05	0.11	0.07	0.04	0.02	0.04	0.02	0.03	0.11	0.05	0.06	0.03
K 2O	0.01	0.00	0.00	0.01	0.00	0.01	0.00	0.02	0.02	0.00	0.01	0.00	0.00	0.00	0.02	0.00	0.00	0.02	0.00	0.00	0.01
Sum	100.43	100.00	99.70	99.80	100.29	100.65	99.80	100.46	99.94	99.97	99.71	99.66	100.14	99.86	99.85	99.88	100.06	100.25	100.45	100.78	100.00
Wo%	0.69	1.45	1.80	1.62	3.12	1.40	3.22	0.63	1.03	0.92	3.34	1.21	1.14	0.80	0.59	0.54	1.08	1.38	1.39	1.41	0.83
En%	89.51	88.81	87.43	87.18	86.12	87.69	86.51	88.16	87.95	89.82	87.30	89.25	90.15	90.02	90.15	90.32	87.73	88.36	88.08	86.19	89.94
Fs%	9.80	9.74	10.77	11.20	10.76	10.90	10.27	11.21	11.03	9.26	9.36	9.54	8.71	9.18	9.26	9.15	11.19	10.26	10.53	12.40	9.24
mg*	0.90	0.90	0.89	0.89	0.89	0.89	0.90	0.89	0.89	0.91	0.91	0.91	0.91	0.91	0.91	0.91	0.89	0.90	0.90	0.88	0.91

*mg** Mg/(Mg + Fetot); *Pr* protogranular texture; *Tr* transitional texture; *Py* pyrometamorphic texture

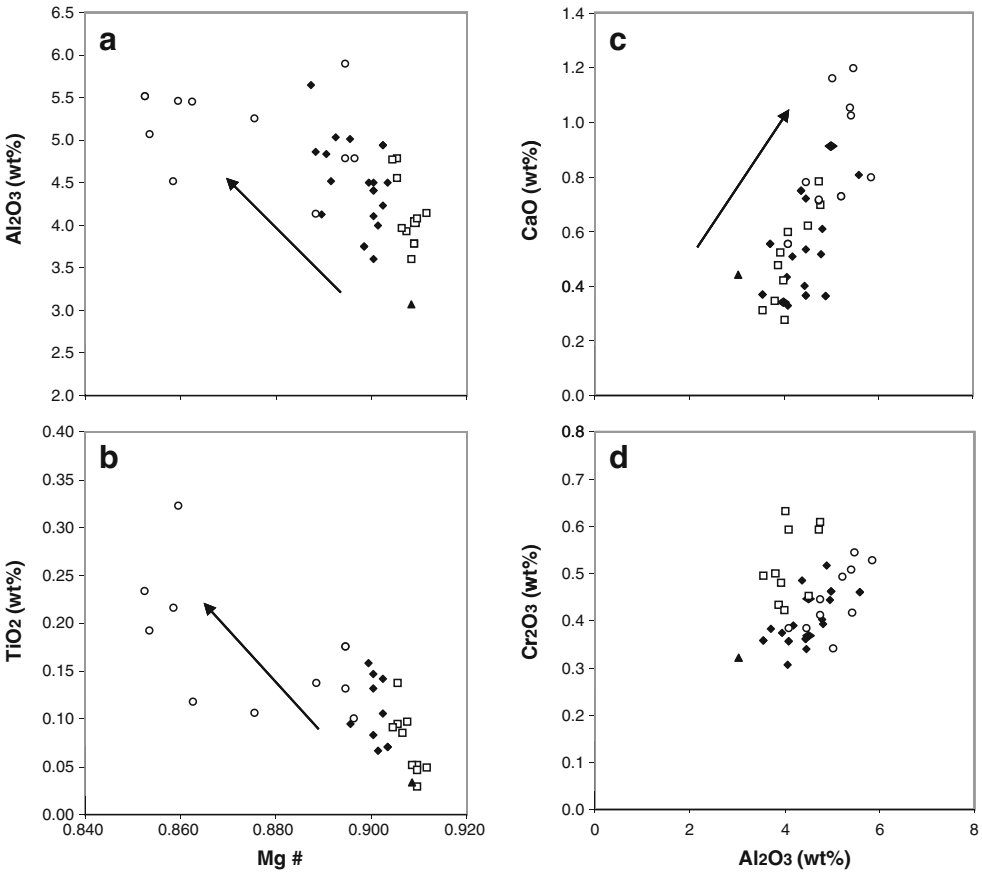

Fig. 5 Al_2O_3 - TiO_2 – CaO - Cr_2O_3 - mg # relationships in orthopyroxene in mantle xenoliths from Veneto Vulcanic Province. Symbols as in Fig. 4

1) Type I early CO_2-rich fluid inclusions, present only in transitional xenoliths, where they occur in the large orthopyroxene and olivine porphyroclasts, isolated or forming small clusters and short intragranular trails (Fig. 8a). Some Type I inclusions in orthopyroxene porphyroclasts contain a birefringent solid (<10 μm) identified as pargasite by SEM analyses (Fig. 8b). Partial decrepitation is common (haloes of small inclusions around the inclusions cavity). Type I fluid inclusions are not associated with the Type A or B silicate glasses;
2) Type II late CO_2-rich fluid inclusions, occurring in trails, commonly present in orthopyroxene, clinopyroxene and olivine in all studied samples (Fig. 8c). Type II fluid inclusions are often associated with silicate-melt inclusions (Type A glass; Fig. 8c). In the core of sieve-clinopyroxene sometimes are present late Type III inclusions, associated to melt inclusions (Type B glass).

Most of the Type I and Type II fluid inclusions melt in a narrow T interval (−57/−56.5°C; highest frequency *Tm*=−56.5°C) as shown in Fig. 9, suggesting nearly pure CO_2. A few among early Type I inclusions show initial melting from −57 to −59°C. No microthermometric measurements were performed in Type III fluid inclusions because of optical problems due to the high porosity of the sieve-clinopyroxene.

In order to identify the additional component that depresses the CO_2 melting temperature, these inclusions were analysed by micro-Raman spectroscopy. Micro-Raman analyses indicate that early Type I CO_2 fluids may contain additional 4–7 mole% CO or graphite. Most Type I CO_2-rich fluid inclusions homogenize to liquid (Th_L), in a large interval of temperature between −44 and 31°C (Fig. 10). The lowest value of Th_L (−44°C) is for a pure CO_2 fluid inclusion and corresponds to a density of 1.132 g/cm^3, indicating a minimum trapping pressure of fluid of 9.4 kbar at 800°C (Fig. 10).

Although homogenization temperatures are similar, Type I and Type II fluid inclusions show distinct chemical composition. While late Type II fluids are pure CO_2 coexisting with Type A melts, early Type I fluids represent complex mixtures of CO_2±CO, and should also have contained some H_2O, as suggested by the presence of pargasite.

Glass chemistry

Type A glass in melt inclusions (Table 5) shows rather constant SiO_2 (59.50–63.27 wt%), Al_2O_3 (19.98–

Table 4 Selected chemical analyses of spinel from VVP xenoliths

Rock	Lherz.	Lherz.	Lherz.	Lherz.	Lherz.	Lherz.	Lherz.	Lherz.	Lherz.	Lherz.	Lherz.	Lherz.	Lherz.	Lherz.	Lherz.	Harz.
Texture	Pr	Pr	Pr	Pr	Pr	Pr	Pr	Tr	Tr	Tr	Tr	Tr	Tr	Py	Py	Tr
Sample	M.Mad.	M.Mad.	M.Mad.	M.Mad.	M.Mad.	M.Mad.	M.Mad.	M.Mad.	M.Mad.	SGIL	SGIL	SGIL	SGIL	SGIL	SGIL	M.Mad.
	1a-1,1	1a-4,1	1a-4,2	22b-3,2	27-2a-3a	27-2a-3d	27-2a-2a	28-3d	28-1a	35-2-6a	35-2-6b	2a-8,1	2a-2,1	2a-11,2	2a-10,2	2b-4,1	7a-9,1	7a-1,7	7a-2,3	7a-2,3	7a-3,3
(wt%)																					
SiO2	0.01	0.02	0.06	0.00	0.03	0.02	0.02	0.01	0.01	0.04	0.03	0.07	0.03	0.06	0.06	0.00	0.06	0.02	0.03	1.03	20.26	8.05
TiO2	0.07	0.05	0.10	0.09	0.05	0.15	0.07	0.10	0.11	0.08	0.11	0.01	0.03	0.01	0.02	0.02	0.00	0.07	0.25	0.65	0.00	0.02
Al2O3	57.01	54.32	53.74	55.56	53.56	52.83	54.14	56.91	56.14	54.95	55.18	49.34	48.97	48.92	47.39	48.28	57.53	46.99	47.15	32.05	42.06
Cr2O3	10.63	12.86	13.17	9.89	13.14	13.85	12.49	10.77	9.53	11.69	12.29	16.03	17.06	15.55	17.68	16.95	8.40	13.56	7.63	12.08	14.55
FeO	10.09	11.35	11.78	11.95	11.92	11.78	11.70	11.91	12.63	10.59	10.07	14.16	12.98	13.59	14.35	13.82	12.44	21.54	21.53	11.13	10.44
Fe2O3	1.12	1.26	1.31	1.33	1.32	1.31	1.30	1.32	1.40	1.18	1.12	1.57	1.44	1.51	1.59	1.53	1.38	2.39	2.39	1.23	1.16
MgO	20.80	19.95	20.43	20.56	19.77	19.98	20.03	18.82	20.17	20.45	20.99	18.93	19.57	19.59	18.89	18.90	19.70	15.87	18.35	24.73	24.24
CaO	0.00	0.00	0.00	0.00	0.02	0.00	0.00	0.00	0.03	0.00	0.00	0.00	0.01	0.04	0.01	0.03	0.00	0.00	0.69	0.18	0.30
Sum	99.73	99.80	100.59	99.37	99.81	99.91	99.76	99.84	100.02	98.96	99.78	100.12	100.08	99.26	99.92	99.56	99.54	100.63	99.41	101.67	100.82
mg*	0.786	0.758	0.756	0.754	0.747	0.751	0.753	0.738	0.740	0.775	0.788	0.704	0.731	0.718	0.697	0.709	0.738	0.568	0.603	0.798	0.805
cr**	0.111	0.137	0.141	0.107	0.141	0.150	0.134	0.113	0.102	0.125	0.130	0.178	0.188	0.175	0.199	0.191	0.089	0.162	0.098	0.202	0.188

*mg** Mg/(Mg + Fe2+); *cr*** Cr/(Cr + Al3+); *Pr* protogranular texture; *Tr* transitional texture; *Py* pyrometamorphic texture

21.67 wt%), and Na_2O (7.06–7.53 wt%), and more variable CaO (1.99–4.21 wt%) and K_2O (2.17–5.45 wt %). Veins and pockets show more variable composition, characterized by higher SiO_2 and K_2O (62.70–66.10 wt% and 4.26–8.21 wt%, respectively), lower CaO (0.39–2.60 wt%), Al_2O_3 (16.74–21.56 wt%) and Na_2O (5.56–7.04 wt%) contents.

Type B glass has a distinct composition (Table 5): low SiO_2 (52.79–53.51 wt%), K_2O (0.21–0.29 wt%), and Na_2O (4.67–4.87 wt%), and high Al_2O_3 (28.42–28.73 wt %), and CaO (11.44–11.76 wt%). Data show that Type A and B glasses have different compositions in terms of CaO, Na_2O and K_2O. The Na_2O/K_2O ratio varies between 0.71 and 3.47 for Type A glass, 15.94 to 23.64 for Type B glass.

P-T-fO2 estimates

Data on temperature, pressure, and oxygen fugacity for VVP xenoliths were calculated from the composition of grains in all the xenoliths; results are reported in Table 6. The origin of all samples is the lithosphere beneath VVP, at P-T conditions within the stability field of spinel. Experimental data show that the minimum pressures for spinel peridotites are constrained by the maximum pressure limit for plagioclase-bearing peridotites (7–8 kbar at 800–1200°C for the NCFMAS system; O'Neill 1981; Gasparik 1987).

Geothermometers applied to the VVP xenoliths include two-pyroxene geothermometer based on diopside and enstatite solubility in coexisting ortho- and clinopyroxene (BK; Brey and Kohler 1990), and the Fe-Mg exchange reaction between olivine-spinel (B; Ballhaus et al. 1991). The temperatures calculated using BK for xenoliths with protogranular and transitional textures range between 742 and 866°C (± 15°C). For spinel peridotites, nominal equilibration pressures were obtained from the temperature independent single-pyroxene barometer (Mercier 1980) to estimate the pressure of the VVP xenoliths. Both the orthopyroxene (P_{opx}) and clinopyroxene (P_{cpx}) equations are used. The estimated pressures range between 8 and 21 kbar (Table 6).

The oxygen fugacity was calculated in protogranular and transitional xenoliths, using the couple olivine-spinel oxygen geobarometer of Ballhaus et al. (1991). The B geothermometer requires an assumption of pressure; we used the pressure of 10 kbar for all samples (the minimum pressure of pure CO_2 fluid inclusions). At the equilibration pressures of 10 kbar, the $\Delta\log(f_{O2})^{FMQ}$ mean value is ~−1.1, within the range of subcontinental mantle field. The possible early Type I fluid composition in transitional xenoliths can be calculated based on temperature,

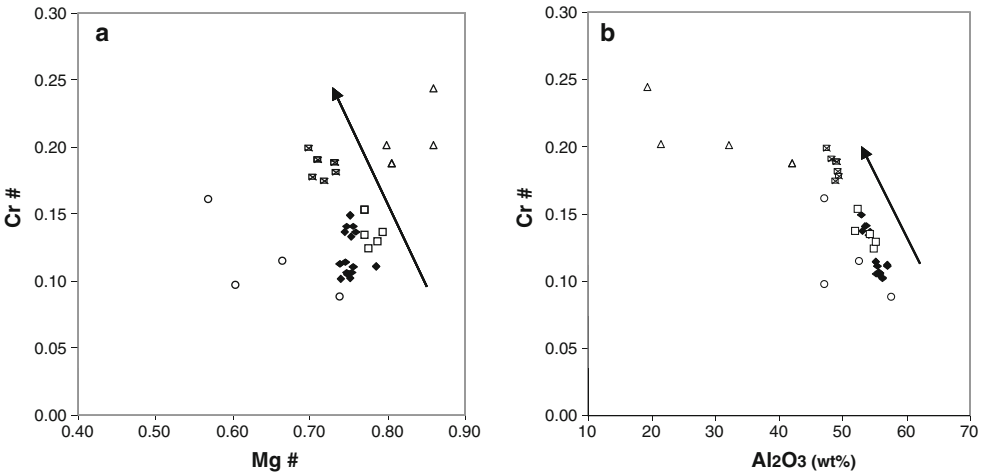

Fig. 6 Al_2O_3 - mg # - cr # relationships in spinel in mantle xenoliths from VVP. Symbols: (*black diamond*) vermicular spinels in protogranular lherzolites; (*white square*) vermicular spinels in transitional lherzolites; (*white triangle*) vermicular spinels in transitional harzburgite; (*white circle*) spongy spinels in pyrometamorphic lherzolite (SG IL 7a); (*squared times*) holly-leaf spinel in transitional lherzolite

pressure, oxygen fugacity conditions, and measured CO_2/CO ratio of fluids (COH system; Huizenga 2005). Such a fluid (when CH_4 absent), is stable at T=800°C, P=10 kbar, $-0.5 \leq \Delta\log(f_{O2})^{FMQ} \leq 1$ (when graphite is absent, $a_{graphite} < 1$) and for a CO_2/CO ratio=13–24 should contain about 20 mole % water (80 mole% of CO_2, 19 mole% of H_2O and 1 mole% of CO). For such a fluid the re-calculated isochore gives similar pressure values of 10.6 kbar.

The lithosphere beneath the VVP sampled by spinel peridotites equilibrated in a temperature range between 742 and 866°C, for a mean value of 800°C, as calculated in protogranular and transitional xenoliths. The equilibration pressures of fluid inclusions at these temperatures range between 9.4 and 10.6 kbar, corresponding to depths between 34 and 38 km. Since in this area the Moho discontinuity is at a depth of about 28 km (Slejko et al. 1987), it results that studied xenoliths came from the uppermost 10 km of the mantle.

Discussion

Depleted mantle beneath the VVP: protogranular xenoliths

The lherzolites with protogranular xenoliths represent the depleted mantle beneath the VVP. In these samples, the clinopyroxene displays negative correlations between Mg # vs. TiO_2, Al_2O_3, and Na_2O and a positive correlation vs. Cr_2O_3 (Fig. 4a-d); the orthopyroxene shows negative correlations between Al_2O_3 and TiO_2 vs. Mg # and positive correlations between CaO and Cr_2O_3 vs. Al_2O_3 (Fig. 5); the spinel is vermicular and has high Al_2O_3 contents and low Cr # (Fig. 6). The clinopyroxene trace element patterns can be used to place constrains on the relative importance of the partial melting process undergone by mantle material. Clinopyroxene from protogranular xenoliths shows MREE and HREE content ~10 times chondrite and depletion in LREE (Fig. 7a), in incompatible elements and in Nb, Sr, Zr and Pb (Fig. 7b), compatible with a depleted mantle. According to Beccaluva et al. (2001), HREE patterns can be explained by a simple fractional melting model, with extraction of about 5–20% basic melts from 10 (lherzolites) to 3 (harzburgite) times chondrite respectively, starting from fertile VVP spinel lherzolite. Recent osmium isotope dating by Goritschnig et al. (2005), suggest that the mantle partial melting age in peridotites from the VVP occurred at 1.2 Gy.

Multi-stage metasomatism transitional xenoliths

A late metasomatic event in the lithosphere beneath the VVP, due to the interaction of mantle rocks with a pervasive metasomatic agent (silicate melt) was previously reported by Siena and Coltorti (1989) (T=1280–1370°C and P=18–20 kbar). This event is preserved only in the strongly reacted xenolith (sample SGIL7a) characterized by sieve-clinopyroxene with the highest contents of TiO_2, Al_2O_3, and Na_2O and low values in Cr_2O_3. In this sample, the orthopyroxene shows the highest values in TiO_2, Al_2O_3, and CaO and high Cr_2O_3 contents; the spinel shows low values in Cr #, Mg # and Al_2O_3. The pattern of trace elements in clinopyroxene in the pyrometamorphic xenolith displays an enrichment in REE, Th, U, and Nb, a depletion in Ba and light negative anomaly in Sr, Ti and Pb, showing affinity with alkaline lavas (alkali basalts, basanites, and nephelinites; Siena and Coltorti 1989; Beccaluva et al. 2001).

The lherzolites in transitional xenoliths preserve additional evidence for an older mantle enrichment event in the lithosphere beneath the VVP. Trace elements in clinopyroxenes show patterns characterized by an enrichment in LREE and spoon-shaped REE patterns, especially evident in the harzburgite, variable

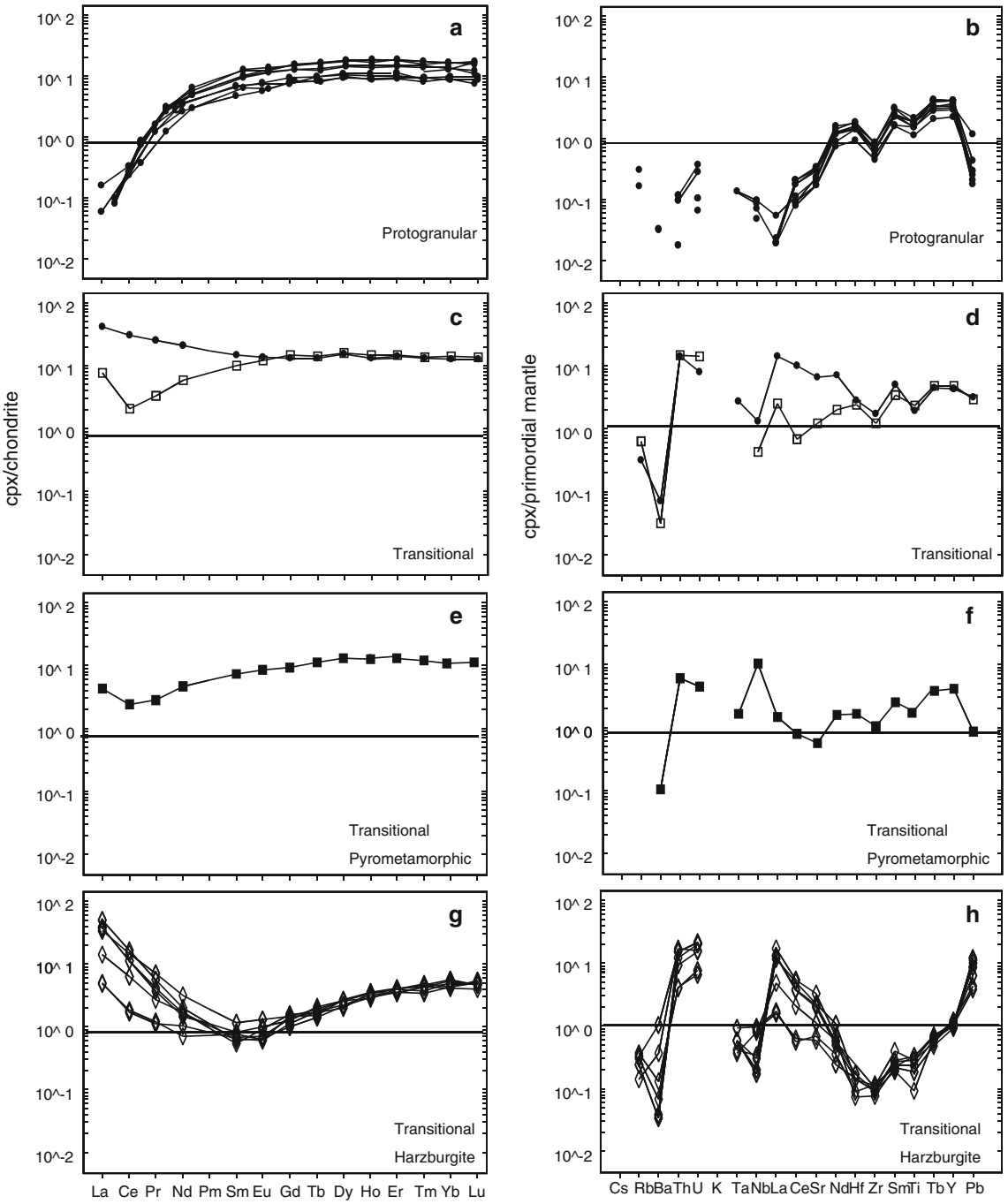

Fig. 7 REE normalised to chondrite (on the left, Sun and McDonough 1989) and incompatible trace elements normalised to primitive mantle (on the right, McDonough et al. 1992) in clinopyroxenes

enrichments in some LILE, depletion in HFSE. The evidence of LREE enrichment, the positive anomalies in Th, U, Sr, and Pb, and the relative depletion in Nb, Ta, Zr, Hf and Ti can have been induced by interaction of mantle rocks with low fractions of basaltic melts or with water-rich fluids or silicate melts.

As discussed by Ionov et al. (2002), the REE spoon-shaped enrichment patterns in mantle minerals could be explained with the increase of melt/fluid percolating distance from a metasomatic melt source, due to the higher migration velocity of LREE respect to HREE, more compatible in the mantle mineralogy. It is also suggested that clinopyroxene-poor system (harzburgite) more rapidly reaches the equilibrium with the melt/fluid than the fertile mantle, due to the higher compatibility of REE in clinopyroxene than orthopyroxene and olivine.

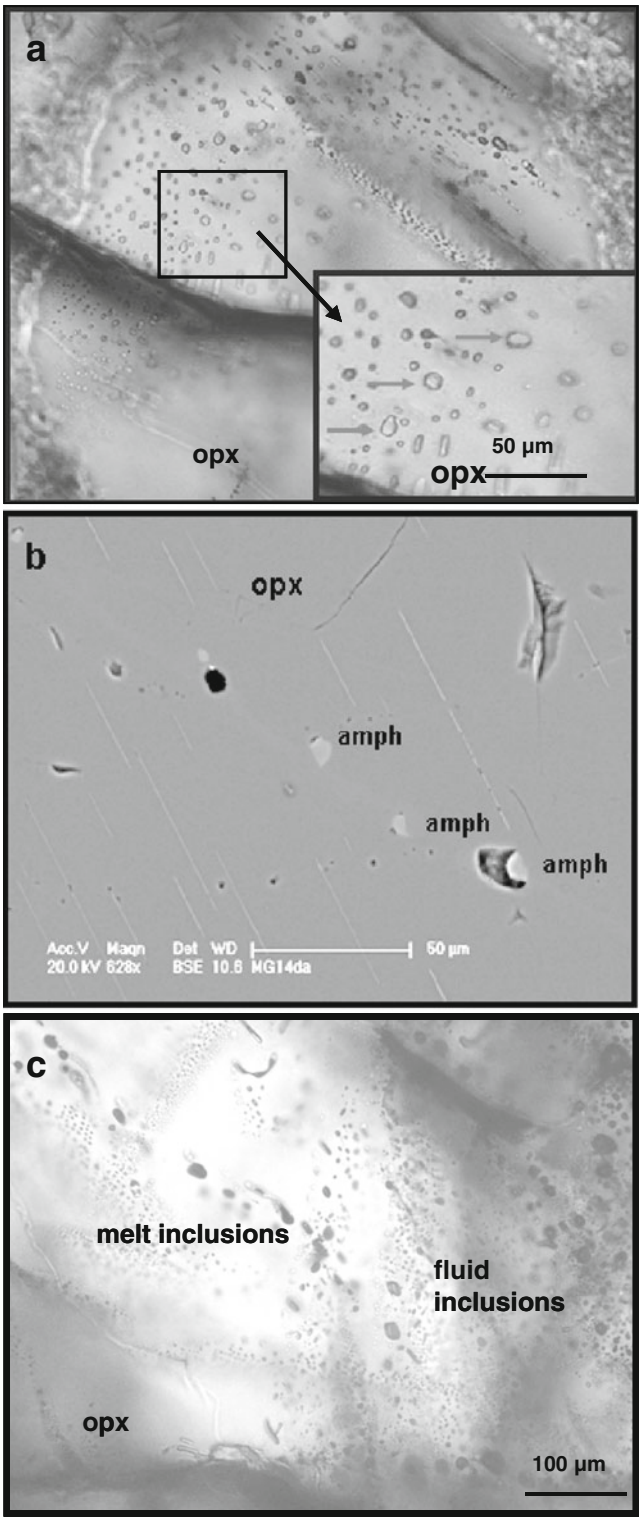

Fig. 8 Microphotographs of fluid inclusions in orthopyroxene in a transitional xenolith: **a**) Type I CO_2 ± CO ± graphite inclusions; **b**) Type I inclusions containing amphibole (3–8 µm) as trapped mineral; SEM image; **c**) Type II pure CO_2 coexisting with Type A melt inclusions

Bedini et al. (1997) and Ionov et al. (2002), explain that the enrichment in some LILE can be due to interaction of

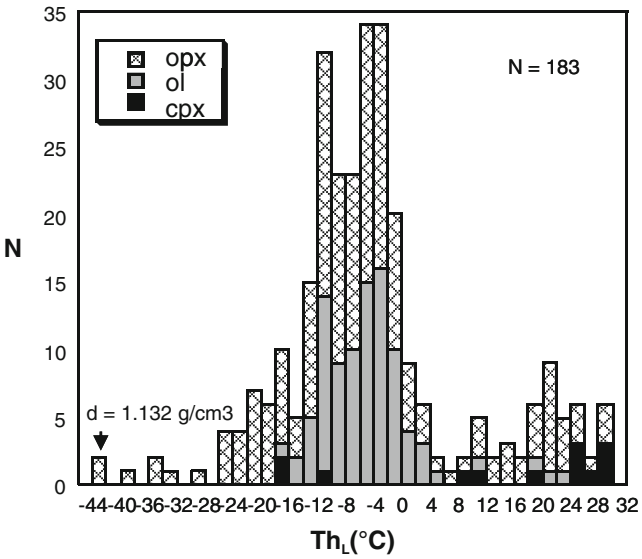

Fig. 9 Histogram showing temperature of homogenization to the liquid phase (Th_L) of fluid inclusions present in mantle xenoliths of VVP: the arrow indicates the highest density value. N = number of measurements

the mantle rock with small fractions of LILE-enriched melts. The negative HFSE anomalies can be related to chromatographic fractionation during porous melt flow

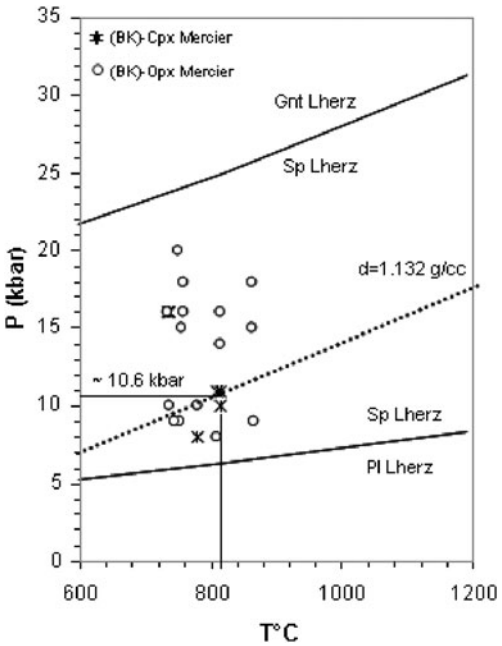

Fig. 10 P-T diagram of VVP reconstructed by mineral geothermometers and fluid geobarometer (*see text*) in protogranular and transitional xenoliths. Isochore shows the densest pure CO_2 corresponding to the minimum trapping fluid pressure (10.6 kbar), for a temperature of 800°C (Brey and Kohler 1990). Estimated nominal equilibration pressures were calculated from the temperature independent single-pyroxene geobarometer of Mercier (1980)

Table 5 Selected chemical analyses of glass from VVP xenoliths

Rock Texture Type Host Sample	Lherz. Pr A MI M.Mad. 1a-7,6	Lherz. Tr A MI SGIL 2a-7,11	Lherz. Tr A MI SGIL 2a-4,4	Lherz. Tr A MI SGIL 2b-4,5	Lherz. Py B MI SGIL 7a-7,3	Lherz. Py B MI SGIL 7a-7,4	Lherz. Pr A Vn M.Mad. 7a-4,8	Lherz. Pr A Vn M.Mad. 7a-1,3	Lherz. Pr A Vn M.Mad. 22b-4,11	Lherz. Tr A Vn SGIL 2a-8,5	Lherz. Pr A Vn M.Mad. 28-4c	Lherz. Pr A Vn M.Mad. 28-4d
(wt%)												
SiO2	59.50	63.27	63.02	61.79	52.79	53.51	66.10	62.70	64.24	65.11	65.12	63.02
Al2O3	19.98	20.92	20.61	21.67	28.73	28.42	19.21	21.56	18.15	16.69	18.41	16.74
TiO2	0.96	0.47	0.17	0.06	0.14	0.18	0.10	0.55	1.27	0.56	0.36	1.13
Cr2O3	0.00	0.00	0.07	0.23	0.00	0.00	0.10	0.00	0.03	0.03	0.02	0.01
FeO	1.73	0.44	0.50	0.42	0.63	0.50	0.21	0.44	1.04	2.35	0.27	1.40
MnO	0.00	0.07	0.00	0.03	0.00	0.00	0.00	0.00	0.00	0.04	0.04	0.07
MgO	1.33	0.41	1.55	0.67	0.69	0.41	0.02	0.03	0.21	1.99	0.15	1.40
CaO	1.99	2.55	4.21	3.76	11.76	11.44	0.44	2.60	0.39	1.15	0.70	0.54
Na2O	7.06	7.14	7.37	7.53	4.67	4.87	6.45	6.67	5.85	5.56	6.55	5.92
K2O	5.45	4.26	3.12	2.17	0.29	0.21	6.89	4.26	8.21	7.10	6.70	6.95
P2O5	0.08	0.16	0.03	0.00	0.05	0.02	0.02	0.07	0.19	0.13	0.00	0.00
F	0.08	0.06	0.00	0.00	0.00	0.00	0.00	0.00	0.01	0.13	–	–
Cl	0.11	0.01	0.00	0.01	0.15	0.10	0.00	0.01	0.02	0.01	0.01	0.00
Totale	98.30	99.73	100.66	98.36	99.91	99.67	99.55	98.89	99.60	101.07	98.37	97.20
mg*	0.43	0.48	0.76	0.61	0.52	0.45	0.07	0.05	0.17	0.46	0.36	0.50
Na2O + K2O	12.51	11.39	10.49	9.70	4.96	5.08	13.34	10.93	14.05	12.66	13.25	12.87
Na2O/K2O	1.30	1.68	2.37	3.47	15.94	23.64	0.94	1.57	0.71	0.78	0.98	0.85

*mg** Mg/(Mg + Fe^{tot}); *Pr* protogranular texture; *Tr* transitional texture; *Py* pyrometamorphic texture;
A = Type A glass; B = Type B glass; *MI* melt inclusions; *Vn* vein

and reactions at decreasing melt mass during percolation of basaltic melts (Takazawa et al. 1992).

However, the observed enrichment in Sr and Pb in transitional xenoliths cannot be explained with the chromatographic effect. As showed by Vannucci et al. (2007), Shibata and Nakamura (1997), and Kosigo et al. (1997), LILE and most incompatible LREE react faster than Sr during reaction porous flow and are transported more easily by melts and/or fluids, due to Sr and Pb higher mobility in aqueous fluid than other elements of similar incompatibility during magmatic processes. For such reason, it is possible that an interaction of mantle rocks beneath the VVP with a water-rich fluids/melts, enriched in Sr and Pb, U, and T has occurred (Maury et al. 1992; Zanetti et al. 1999).

Type I fluid inclusions, containing amphibole, preserve the metasomatic agent that characterize the older metasomatic event in the mantle beneath the VVP. The hydrous metasomatism is cryptic because there was no introduction of hydrous phases to the lherzolites, although presence of pargasite in the carrier fluid/melt is indicated by fluid inclusions, and by occasional findings in xenoliths (Morten 1979). Presence of amphibole would suggest a melt like hydrous metasomatic agent, more than a free aqueous fluid.

Most of the mantle rocks from the VVP display the transitional texture, which indicate that major mantle deformation was associated to the hydrous enrichment events. This event may be related to the Alpine subduction. Similar conclusions were also proposed by Gasperini et al. (2006), based on whole-rock LILE enrichment and HFSE depletion.

Conclusions

The mantle beneath the VVP equilibrated in a temperature range between 742 and 866°C. For a mean value of 800°C, the densest Type I pure CO_2 fluid inclusions (d=1.132 g/cm^3) corresponds to a minimum trapping pressure of 9.4 kbar (34 km). From the fluid inclusions CO and C additional content, the possible original fluid composition can be determined as 80 mole% of CO_2, 19 mole% of H_2O, and 1 mole% of CO. For such fluid the calculated isochore gives 10.6 kbar (38 km).

Table 6 Equilibrium temperatures, pressures, and oxygen fugacity values for mantle xenoliths from VVP

	BK; 1990	M; (1980)			B; (1991) at 10 kbar	
	T (°C)	Pcpx (kbar)	Popx (kbar)		T (°C)	Δlog (fo2)FMQ
Cpx/Opx				Ol/Spl		
MMad1a				MMad1a		
1) coarse grain	742			1) -	836	−1.69
3) exsol.cpx in opx	808			2) -	766	−1.49
MMad7a (Harzb.)		11	8	3) -	767	−0.93
1) exsol.cpx in opx	745			MMad7a (Harzb.)		
3) exsol.cpx in opx	815			1) -	867	−1.67
MMad22b				2) -	867	−1.67
1) coarse grain	756	10	16	3) -	811	−1.43
2) coarse grain	757			MMad22b		
3) coarse grain	752		15	1) -	992	−1.74
4) coarse grain	862		18	1) -	737	−0.76
5) coarse grain	863		9	1) -	737	−0.76
6) coarse grain	866		15	MMad27-2A		
MMad27-2A			18	1) -	754	−0.89
1) coarse grain	733		9	2) -	772	−0.96
2) coarse grain	742			3) -	754	−0.87
3) coarse grain	736			4) -	732	−0.83
4) coarse grain	838			5) -	754	−0.87
5) coarse grain	848			6) -	732	−0.83
6) coarse grain	840			MMad28		
SGIL7a *(pyr)*				1) -	769	−0.95
1) cpx sieve	1132			2) -	747	−0.90
1) cpx sieve	1133			6) -	755	−0.89
1) cpx sieve	1159			MMad35-2		
1) cpx sieve	1084			1) -	801	−1.68
1) cpx sieve	1079	11	14	2) -	778	−2.01
1) cpx sieve	1041		16	3) -	827	−1.81
1) cpx sieve	995					
8) cpx in opx	1171					

BK Brey and Kohler (1990); *B* Ballhaus et al. (1991); *M* Mercier (1980);
Δlog(fo2)FMQ = olivine – spinel oxygen geobarometer of Ballhaus et al. (1991)

A major metasomatic event, induced melting and re-crystallisation with variable LREE enrichment in mantle rocks, due to infiltration of alkali silicate basic melts at high temperatures (related to the Tertiary volcanism), as also described by Beccaluva et al. (2001). Type A glass inclusions represent the metasomatic agent, enriched in SiO_2 and alkalis, while Type B glass formed during melting of clinopyroxene, resulting in sieve textures.

Although interaction with metasomatic melts related to Tertiary volcanism in the area has been pervasive, present study suggests that an older metasomatic event induced by water-rich fluids or silicate melts occurred in the lithosphere beneath the VVP, probably during Alpine subduction. Presence of amphibole in some Type I fluid inclusions in orthopyroxenes from transitional xenoliths suggest a melt-like hydrous metasomatic agent. In this hypothesis LREE enrichment and negative anomalies of Nb, Ta, Hf, Zr, and Ti, and a significant enrichment in Th, U, Pb, Ba and Sr in clinopyroxenes from transitional samples (especially in the harzburgite), may indicate transport by aqueous fluids.

Acknowledgements Constructive comments by two anonymous reviewers contributed to the improvement of this paper.

References

Bakker RJ (2003) Computer programs for analysis of fluid inclusion data and for modelling bulk fluid properties. Chem Geol 194:3–23

Ballhaus C, Berry RF, Green DH (1991) High pressure experimental calibration of the olivine-orthopyroxene-spinel oxygen geobarometer: implications for the oxidation state of the upper mantle. Contrib Mineral Petrol 107:27–40

Barbieri G, De Zanche V, Medizza F, Sedea R (1982) Considerazioni sul vulcanismo terziario del Veneto Occidentale e del Trentino Meridionale. Rend Soc Geol It 4:267–270

Barbieri G, De Zanche V, Sedea R (1991) Vulcanismo Paleogenico ed evoluzione del semigraben Alpone-Agno. Rend Soc Geol It 14:5–12

Beccaluva L, Bonadiman C, Coltorti M, Salvini L, Siena F (2001) Depletion events, nature of metasomatizing agent and timing of enrichment processes in lithospheric mantle xenoliths from the Veneto Volcanic Province. J Petrol 42:173–187

Bedini RM, Bodinier JL, Dautria JL, Morten L (1997) Evolution of LILE-enriched small melt fractions in the lithospheric mantle: a case study from the East Africa Rift. Earth Planet Sci Lett 153:67–83

Bianchini G, Beccaluva L, Siena F (2008) Post-collisional and intraplate Cenozoic volcanism in the rifted Apennines/Adriatic domain. Lithos 101:125–140

Bonadiman C, Coltorti M, Dilani L, Salvini L, Siena F, Tassinari R (2001) Metasomatism in the lithospheric mantle and its relationships to magmatism in the Veneto Volcanic Province, Italy. Period Mineral 70:333–357

Brey GM, Kohler T (1990) Geothermobarometry in four-phase lherzolites II. New thermobarometers, and practical assessment of existing themobarometers. J Petrol 31:1353–1378

Coltorti M, Beccaluva L, Bonadiman C, Salvini L, Siena F (2000) Glasses in mantle xenoliths as geochemical indicators of metasomatic agents. Earth Planet Sci Lett 183:303–320

De Vecchi G, Sedea R (1995) The paleogene basalts of the Veneto region (NE Italy). Mem Sci Geol Univ Padova 47:281–303

De Vecchi G, Gregnanin A, Piccirillo EM (1976) Tertiary volcanism in Veneto: magmatology, petrogenesis, and geodynamic implications. Geol Rundschau 65:701–710

Frezzotti ML, Tecce F, Casagli A (2011) Raman spectroscopy for fluid inclusion analysis. J Geochem Explor. doi:10.1016/j.gexplo.2011.09.009

Galassi B, Monese A, Ogniben G, Siena F, Vaccaro C (1994) Age and neture of lamprophyric dikes at Calceranica (Trento). Miner Petr Acta 37:163–171

Gasparik T (1987) Orthopyroxene thermobarometry in simple and complex systems. Contrib Mineral Petrol 96:357–370

Gasperini D, Bosch D, Braga R, Bondi M, Macera P, Morten L (2006) Ultramafic xenoliths from the Veneto Volcanic Province (Italy): petrological and geochemical evidence for multiple metasomatism of the SE Alps mantle lithosphere. Geochem J 40:377–404

Goritschnig B, Braga R, Meisel T, Mogessie A, Morten L (2005) Osmium Isotopic composition and platinum group abundances of mantle xenoliths from the Adige Valley, Northern Italy Geophys. Res Abstr 7:06059

Holloway JR (1977) Fugacity and activity of molecular species in supercritical fluids. In: Fraser DG (ed) Thermodynamics in Geology. Reidel, Dordrecht, pp 161–181

Huizenga JM (2005) COH, an excel spreadsheet for composition calculations in the C-O-H fluid system. Comput Geosci 31:797–800

Ionov DA, Bodinier JL, Mukasa SB, Zanetti A (2002) Mechanisms and sources of mantle metasomatism: major and trace element compositions of peridotite xenoliths from Spitsbergen in the context of numerical modelling. J Petrol 43:2219–2259

Kosigo T, Tatsumi Y, Nakano S (1997) Trace elements transport during dehydration processes in the subducted ocean crust: 1. Experiments and implications for the origin of ocean island basalts. Earth Planet Sci Lett 148:193–205

Longerich HP, Jackson SE, Gunther D (1996) Laser ablation inductively coupled plasma mass spectrometric transient signal data acquisition and analyte concentration calculation. J Anal Atom Spectrom 11:899–904

Macera P, Gasperini D, Ranalli G, Mahatsente R (2008) Slab detachment and mantle plume upwelling in subduction zones: an example from the Italian South-Eastern Alps. J Geodyn 45:32–48

Maury RC, Defant MJ, Joron JL (1992) Metasomatism of the sub-arc mantle inferred from trace elements in Philippine xenoliths. Nature 360:661–663

McDonough WF, Sun SS, Ringwood AE, Jagoutz E, Hofmann AW (1992) Potassium, rubidium and cesium in the earth and moon and the evolution of the mantle of the earth. Geochim Cosmochim Ac 56:1,001–1,012. doi:10.1016/0016-7037(92)90043-I

Mercier JCC (1980) Single-pyroxene thermobarometry. Tectonophysics 70:1–37

Mercier JCC, Nicolas A (1975) Texture and fabrics of upper-mantle peridotites as illustrated by xenoliths from basalts. J Petrol 16:454–487

Morten L (1979) Salic, mafic, and ultramafic inclusions and megacrysts in basaltic rocks from M. Lessini, Veneto Region, North Italy. Period Miner 48:75–91

Morten L (1987) Italy: A review of xenolithic occurrences and their comparison with Alpine peridotites. In: Nixon PH (ed) Mantle Xenoliths., pp 135–148

Morten L, Bondi M (1981) Spinel lherzolite inclusions in basalts from Monti Lessini, Veneto Region, northern Italy. N Jb Miner Mh 7:308–316

O'Neill HStC (1981) The transition between spinel lherzolite and garnet lherzolite, and its use as a geobarometer. Contrib Mineral Petrol 77:185–194

Petrelli M, Perugini D, Poli G, Peccerillo A (2007) Graphite electrode tetraborate fusion for automated trace element determination in bulk samples by laser ablation ICP–MS. Microchim Acta 158:275–282

Petrelli M, Perugini D, Alagna KE, Poli G, Peccerillo A (2008) Spatially resolved and bulk trace element analysis by laser ablation – inductively coupled plasma–mass spectrometry (LA–ICP–MS). Per Mineral 77:3–21

Piccoli G, Sedea R, Bellati R, Di Lallo E, Medizza F, Girardi A, De Pieri R, De Vecchi G, Gregnanin A, Piccirillo EM, Norinelli A, Dal Prà A (1981) Note illustrative della carta geologica dei Colli Euganei. Mem Sci Geol 34:523–566

Shibata T, Nakamura E (1997) Across-arc variations of isotope and trace element compositions from Quaternary basaltic volcanic rocks in northeastern Japan: implications for interaction between subducted slab and mantle wedge. J Geoph Res 102:8051–8064

Siena F, Coltorti M (1989) Lithospheric mantle evolution: evidences from ultramafic xenoliths in the Lessinian volcanics (Northern Italy). Chem Geol 77:347–364

Siena F, Coltorti M (1993) Thermobarometric evolution and metasomatic processes of upper mantle in different tectonic settings: evidence from spinel peridotite xenoliths. Eur J Mineral 5:1073–1090

Slejko D, Carulli GB, Carraro F, Castaldini D, Cavallin A, Doglioni C, Iliceto V, Nicolich R, Rebez A, Semenza E, Zanferrari A, Zanolla A (1987) Modello sismotettonico dell'Italia nord-orientale. C.N.R., Gruppo Nazionale Difesa dai Terremoti

Sun SS, McDonough WF 1989 Chemical and isotopic systematics of oceanic basalts: implications for mantle composition and process. In Saunders AD, Norry MJ (eds) Magmatism in the Oceanic Basins. Geological Society, London Special Publication 42: 313–346

Takazawa E, Frey FA, Shimizu N, Obata M, Bodinier JL (1992) Geochemical evidence for melt migration and reaction in the upper mantle. Nature 359:55–58

Vannucci R, Tiepolo M, Defant MJ, Kepezhinskas P (2007) The metasomatic record in the shallow peridotite mantle beneath Grenada (Lesser Antilles arc). Lithos 99:25–44

Zanetti A, Mazzucchelli M, Rivalenti G, Vannucci R (1999) The Finero phlogopite-peridotite massif: an example of subduction-related metasomatism. Contrib Mineral Petrol 134:107–122